ACS Photonics

Open Access

This article is licensed under CC-BY 4.0

pubs.acs.org/journal/apchd5

Article

Two-Dimensional Photonic Crystal Cavities in ZnSe Quantum Well Structures

Siqi Qiao,* Nils von den Driesch, Xi Chen, Stefan Trellenkamp, Florian Lentz, Christoph Krause, Benjamin Bennemann, Thorsten Brazda, Jeremy Witzens, James M. LeBeau, and Alexander Pawlis*

Cite This: *ACS Photonics* 2024, 11, 3545−3553

Read Online

ACCESS | Metrics & More | Article Recommendations | Supporting Information

ABSTRACT: ZnSe and related materials like ZnMgSe and ZnCdSe are promising II−VI host materials for optically mediated quantum information technology such as single photon sources (SPS) or spin qubits. Integrating these heterostructures into photonic crystal (PC) cavities enables further improvements, for example, realizing Purcell-enhanced SPS with increased quantum efficiency. Here, we report on the implementation of two-dimensional (2D) PC cavities in strained ZnSe quantum wells on top of a novel AlAs supporting layer. This approach overcomes typical obstacles associated with PC membrane fabrication in strained materials, such as cracks and strain relaxation in the corresponding devices. We demonstrate the attainment of the required mechanical stability in our PC devices, complete strain retainment, and effective vertical optical confinement. The structural analysis of our PC cavities reveals excellent etching anisotropy. Additionally, elemental mapping in a scanning transmission electron microscope confirms the transformation of AlAs into AlO_x by postgrowth wet oxidation and reveals partial oxidation of ZnMgSe at the etched sidewalls in the PC. This knowledge is utilized to tailor finite domain time difference simulations and to extract the ZnMgSe dispersion relation with small oxygen content. Optical characterization of the PC cavities with cross-polarized resonance scattering verifies the presence of the cavity modes. The excellent agreement between simulation and measured cavity mode energies demonstrates the wide tunability of the PC cavity and proves the pertinence of our model. This implementation of 2D PC cavities in the ZnSe material system establishes a solid foundation for the future development of ZnSe quantum devices.

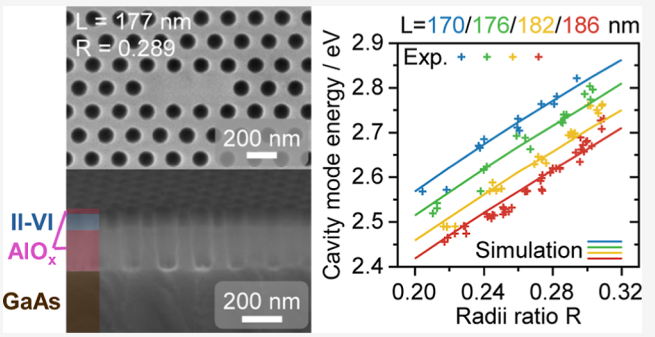

KEYWORDS: *II−VI semiconductor, ZnSe quantum well, photonic crystal cavity, cavity mode, Q-factor, cross-polarized resonance scattering spectroscopy*

Downloaded via RWTH AACHEN HOCHSCHUL BIBL on January 15, 2025 at 07:44:41 (UTC).
See https://pubs.acs.org/sharingguidelines for options on how to legitimately share published articles.

INTRODUCTION

Photonic crystal structures, which are characterized by periodic variations in their refractive indices, possess the ability to modulate light generation and propagation by engineering the photonic band gap. Due to their small mode volume and moderately high *Q*-factor, PC cavities are particularly intriguing to enable substantial emission rate enhancement via the Purcell effect,[1,2] which is primarily determined by the *Q*-factor-to-mode volume ratio. Therefore, PC cavities are used within diverse applications, such as enhancement of the internal quantum efficiency of single photon sources,[3] realization of compact high-resolution on-chip spectrometers,[4] PC lasers,[5,6] and the generation of polaritons for explorations in cavity quantum electrodynamics.[7]

The main challenge of PC cavity fabrication lies in the periodic features, such as the holes, which need to scale with the target wavelength, yielding small lattice constants and consequently small hole radii for the UV-to-green spectral range. So far, numerous PC cavities have been developed covering the whole spectral range from VIS into UV using Si[8] and III−V semiconductors.[9−15] For II−VI semiconductors, PCs have only been realized in ZnO-based heterostructures[6,16,17] operating in the near-UV spectral range. However, to our knowledge, PC cavities have not yet been implemented in the selenides (e.g., ZnSe, MgSe, and CdSe), which are able to bridge the spectral gap between the near-UV and the green spectral range.

Especially, ZnSe- and (Zn,Mg)Se-based heterostructures provide a large direct band gap and high oscillator strength. The minimal lattice mismatch (about 0.2%) between ZnSe and GaAs allows for nearly defect-free growth of ZnSe on standard GaAs substrates. More complex structures, implementing ZnSe QWs between ternary (Zn,Mg)Se barriers, enable even more

Received: February 26, 2024
Revised: August 7, 2024
Accepted: August 7, 2024
Published: August 15, 2024

© 2024 The Authors. Published by American Chemical Society

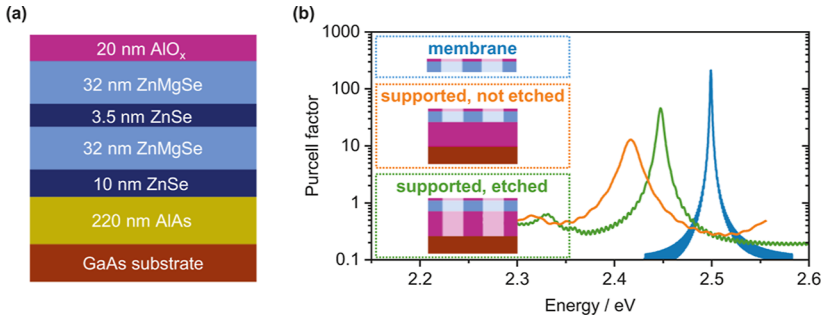

Figure 1. (a) Scheme of the heterostructure layer stack from which the PC cavities are fabricated. (b) Comparing simulated Purcell factors for three different vertical designs (as sketched in the inset) using an unmodified L3 PC cavity (a PC cavity design with three holes missing in the center).

intensive emission, smaller line widths, and the opportunity of spectral tuning by quantum well (QW) engineering.[18,19] Moreover, substitution of the ZnSe QW with one containing (Zn,Cd)Se also allows for accessing the full visible spectral range from blue to yellow.[20,21]

Besides these aspects, ZnSe and related materials have demonstrated enormous potential for modern quantum optical devices, such as indistinguishable SPS[22−25] and optically controlled spin qubits.[26−28] Kutovyi et al.[19] demonstrated highly efficient nanopillar-based SPSs using the donor-bound exciton emission from Cl-donors in ZnSe QWs. Without the presence of any back-reflector in these structures, the external quantum efficiency was strongly enhanced by a factor of 2.5 when tailored solid immersion nanolenses were fabricated on top of the nanopillars. Very recently, Jiang et al.[29] demonstrated Purcell enhancement of the emission from a ZnSe-based SPS by fabrication of Bulls-eye cavities. Further improvement of the external quantum efficiency of such SPSs is feasible via both Purcell enhancement and far-field tailoring when integrating the SPSs into PC cavities. Moreover, this approach enables new perspectives to investigate the nature of exciton−photon interaction with ZnSe or ZnCdSe QWs or CdSe QDs implemented in a 2D- or 3D-photonic confinement instead of the 1D-photonic confinement studied so far.[30−32]

In this work, we present the implementation of two-dimensional PC cavities in the ZnSe QW heterostructures. Instead of adopting the common membrane design, the realization of which leads to strain relaxation and mechanical deformation in our material system, we chose a design with an underlying supporting layer, as similarly presented in the literature.[10,33−35] The pseudomorphically strained ZnSe/(Zn,Mg)Se heterostructures are grown on top of an AlAs buffer layer, which is postgrowth wet oxidized into amorphous oxide. This approach offers not only mechanical stability and strain retainment but also moderately high index guiding for optical confinement in the vertical direction. The fabricated PC cavities were then subjected to structural and elemental analysis to investigate the impact of the fabrication process. Optical characterization of the PC cavities using cross-polarized resonance scattering (RS) spectroscopy provides experimental evidence of the cavity modes. In order to refine the dielectric dispersion and to demonstrate the possibility of individual tunability of the cavity mode energy, we studied a large number of photonic crystals with varying dimensions and confirmed the experimental results by optical simulations using the finite domain time difference (FDTD) method.

METHODS

We will first focus our discussion on a typical heterostructure, which is composed of a ZnSe QW enclosed in ZnMgSe barriers grown on top of an AlAs buffer layer. The overall layer stack is schematically shown in Figure 1a. First, using molecular beam epitaxy (MBE), a roughly 220 nm thick AlAs buffer was grown on the GaAs-(001) substrate. After III−V growth, the sample was transferred in situ (maintaining continuous UHV conditions) to the II−VI MBE chamber, in which the ZnSe/ZnMgSe heterostructure is grown. The latter consists of a 10 nm thick ZnSe buffer and 32 nm thick $Zn_{0.91}Mg_{0.09}Se$ barriers enclosing a 3.5 nm ZnSe QW. Finally, the sample is further transferred into an atomic layer deposition tool and capped with 20 nm AlO_x. Note that due to the larger lattice constants of ZnSe and ZnMgSe compared to GaAs, the overall II−VI heterostructures and also the AlAs buffer layer grow pseudomorphically on the GaAs substrate. The overall lattice relaxation of the QW is about 2%, as confirmed by an XRD reciprocal space map shown in the Supporting Information , Section S1. This low value of strain relaxation indicates a negligible number of misfit dislocations in the whole heterostructure.

In addition to the heterostructure, the design of the PC cavity also plays a crucial role in determining important parameters, such as the Q-factor and mechanical stability. Therefore, we used the commercial FDTD solver Lumerical to perform FDTD simulations for three different vertical PC designs shown in the inset of Figure 1b, namely a free-standing membrane structure, a supported structure with intact underlying AlO_x buffer, and a supported structure with the underlying AlO_x buffer etched through.

The simulations were carried out by assuming a design of an unmodified L3 cavity (PC cavity with three holes missing in the center) with a lattice constant of 175 nm and a radii ratio (i.e., radius/lattice constant) of 0.26. We have chosen the L3 cavity design, as this one yields the highest Purcell factor compared to that of the H1 and L5 configurations with the same hole and lattice geometry. For the purpose of comparison, we restrict ourselves to the selection of a single specific mode (mode 1, see Figure 4a for details). In the simulation model, we assumed for the overall II−VI semiconductor heterostructure the same refractive index dispersion, i.e., corresponding to a 72 nm thick layer entirely composed of ZnMgSe. The approximation is valid because of the low Mg content of 9% and the large volume fraction of 73% ZnMgSe in the whole layer stack. It also gives an adequate fit of the overall heterostructure model (composed of a ZnSe buffer and QW and ZnMgSe barriers) obtained from ellipsometry measurements. Since there is no systematic experimental data available for the dispersion relation of

https://doi.org/10.1021/acsphotonics.4c00340
ACS Photonics 2024, 11, 3545−3553

arbitrary ZnMgSe compounds, we determined the refractive index $n(E)$ using the equations for a single-effective oscillator (SEO) model from ref 36

$$n(E)= \sqrt{1 + \frac{F_0 {E_0}^2}{{E_0}^2 - E^2} + \frac{0.005 {E_g}^2 ({E_g}^2 - E^2)}{({E_g}^2 - E^2)^2 + f_0^2 E^2}}$$

(energy unit: eV)

$$F_0 = -0.078x^2 - 1.552x + 4.899;\ E_0 = 0.385x^2 + 0.754x + 5.207 \quad (1)$$

with F_0 and E_0 representing the effective oscillator strength and band gap of the SEO model, respectively, and $f_0 = 0.02$ eV is related to the line width of the band edge resonance. We modified only the third term in the square root into a Lorentz oscillator to avoid divergence near the ZnMgSe band gap energy E_g. At low temperatures, we assumed $E_g = 2.82 + 1.28x$ (eV), as reported in ref 37, where x represents the Mg concentration. The imaginary part of the dispersion relation is automatically generated in the FDTD solver via the Kramers–Kronig relation and is negligible, except for photon energies close to the ZnMgSe band gap energy. More details can be found in Section S2 of the Supporting Information.

For the dispersion relation of the wet-oxidized former AlAs-buffer layer (and also for the AlO_x capping layer), we used values from the Tauc–Lorentz model, as this model provides the most accurate fit for the heterostructures according to ellipsometry measurements. Hereby, we assume a negligible absorption coefficient in the material. The obtained refractive index (see Supporting Information Section S2) is close to that reported by refs 38 and 39 for wet-oxidized former AlAs into amorphous oxide. At a wavelength of 440 nm, the corresponding refractive indices of $Zn_{0.91}Mg_{0.09}Se$, oxide buffer, and GaAs[40] are 2.78, 1.66, and $5.00 + 1.07i$, respectively, forming index guiding in the vertical direction in case of the supported design with intact oxide buffer below, though weaker than that of the standard membrane design.

The simulation results are shown in Figure 1b and Table 1. The membrane structure provides the strongest index guiding of all three designs, which is verified by the largest Q-factor of 1800. However, the fabrication of such a membrane design from our layer stack is experimentally challenging and hardly feasible. Under-etching the material below the ZnSe/ZnMgSe heterostructure induces relaxation of the residual compressive strain in the overall layer stack, which leads to the formation of extended defects and cracks in the PC structure. On the other hand, the supported design with full oxide buffer provides good mechanical stability but suffers from poor index guiding, causing radiation losses into the substrate. As a result, a Q-factor of only 140 is achieved in this case. Aiming for a compromise between mechanical stability and vertical optical confinement, we opt for a design in which the holes of the photonic crystals are also etched through the underlying oxide buffer. The etching reduces the effective refractive index and therefore enhances the optical confinement in the II–VI layers, which results in an increased Q-factor of 410. Following our simulations, the mode's Purcell factor can exceed 40 in the case of the supported and etched cavity design. Therefore, an overall increase of the extraction efficiency by roughly a factor of 2 compared to that of the Bulls-eye cavities in ref 29 is possible if the side-wall roughness in our structures can be significantly reduced. For this configuration, we tried further optimization in the horizontal L3 cavity design by modification of the three inner hole pair positions, yielding a slightly increased Q-factor of 480 for mode 1. The effect of enhancement is small since the main loss channel in this case is the optical leakage into the AlO_x layer instead of the optical leakage via scattering at the cavity end-holes. For modes 2–5 observed in our simulations, appropriate tailoring of the inner hole displacements may substantially increase the Q-factor from 150 up to about 800. However, in comparison, a much larger enhancement of the Q-factor in membrane PC cavities can be achieved by shifting the three inner hole pairs, which serves as soft tuning of end-hole scattering. In the current investigations, we focus on the unmodified L3 cavity as our preferred PC cavity design.

Table 1. Simulation Results for the Three Different Vertical Designs

design	E_{mode}/eV	Q	V_{mode}/nm^3	F_P[a]
membrane	2.499	1800	4.0×10^6	210
supported, not etched	2.417	140	6.2×10^6	13
supported, etched	2.447	410	4.7×10^6	46

[a]Purcell factor is calculated with the formula $F_P = \frac{3}{4\pi^2}\frac{Q}{V_{mode}}\left(\frac{\lambda}{n}\right)^3$, which provides the maximum Purcell enhancement with an ideally positioned and oriented resonant dipole source. Here, in the formula, λ is the cavity mode wavelength and n is the refractive index of ZnMgSe at λ.

The device fabrication process employs a top-down technique, briefly summarized in the following (see Supporting Information Section S3 for details). First, 40 nm Cr is deposited on the pristine layer stack as a hard mask. Second, the PC cavity design is defined using e-beam lithography. The pattern is then transferred into the Cr layer by using reactive ion etching (RIE) with a gas combination of Cl_2/O_2. Next, several successive etching steps are performed, starting with wet-chemical etching of the AlO_x capping layer using developer AZMIF326. Then, RIE dry etching with H_2/Ar and $Cl_2/Ar/CH_4$ chemistry is applied for etching through the ZnSe/ZnMgSe heterostructure and AlAs layer, respectively. Subsequently, the sample undergoes wet oxidation in a reaction chamber at 350 °C using water vapor carried by nitrogen gas flow. After wet oxidation, the 220 nm thick AlAs buffer is transformed into roughly 190 nm thick AlO_x (shrinkage ratio of 86%, similar to reported values[41,42]), where the shrinkage is validated by means of ellipsometry measurements and scanning electron microscopy (SEM). Finally, the Cr hard mask is removed by subsequent utilization of the O_2 and Cl_2/O_2 plasma.

RESULTS AND DISCUSSION

Figure 2a presents a top-view SEM image of a typical PC cavity after completion of the above-mentioned fabrication process. By fitting circle sizes and center positions of a zoom-in micrograph, we determine the average hole diameter d, average lattice constant L, and therefore the average radii ratio $R = d/2L$ for each individual PC cavity, which is later optically characterized (see Supporting Information Section S4 for details of the fitting process). For the PC cavity shown in Figure 2a, the corresponding parameters are $d = (102 \pm 4)$ nm, $L = (177 \pm 4)$ nm, and $R = 0.289 \pm 0.013$. A cross-sectional SEM micrograph of the PC cavity, shown in Figure 2b, demonstrates nearly vertical sidewalls and good anisotropy of the applied etching processes.

https://doi.org/10.1021/acsphotonics.4c00340
ACS Photonics 2024, 11, 3545–3553

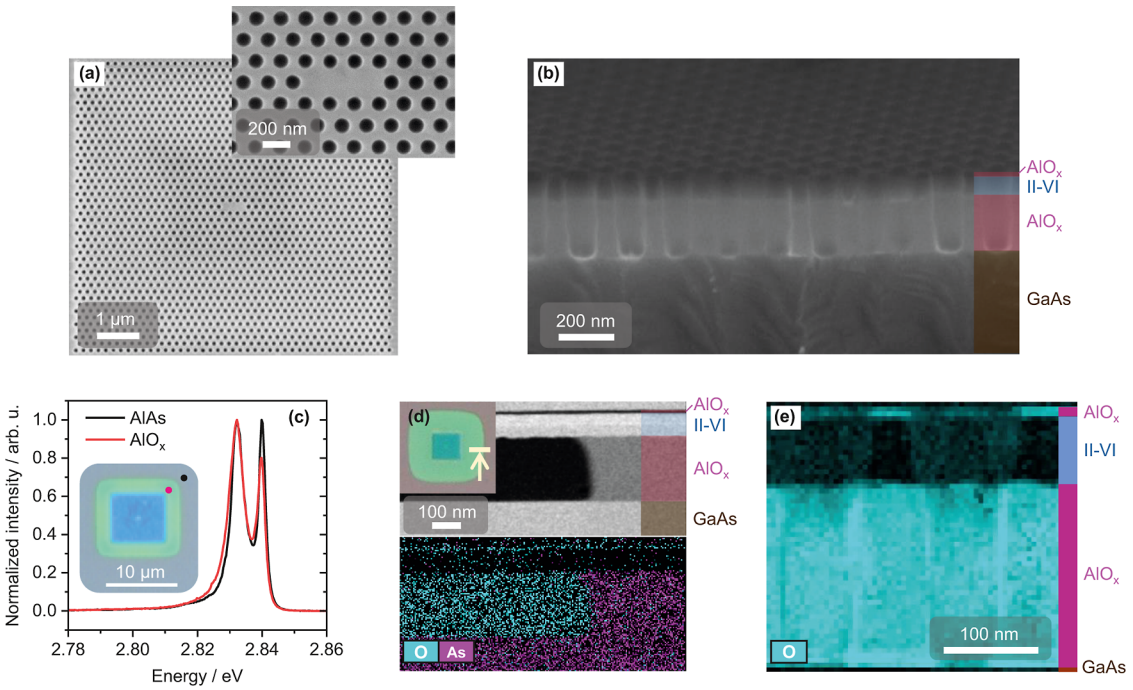

Figure 2. SEM and TEM characterization of a typical fabricated sample. (a) Top-view SEM micrograph of a PC cavity after processing. The zoomed-in inset shows the cavity region. (b) Cross-sectional SEM micrograph of a PC cavity of the same design revealing the clear interface boundaries between the stack materials. (c) Photoluminescence (PL) spectra of the pristine region of the sample (black spot in the inset) with AlAs below, and of the wet-oxidized region of the sample (red spot) with the AlO_x layer below the II−VI material, respectively. The inset shows the optical micrograph around one typical PC cavity. (d) Cross-sectional high-angle annular dark-field (HAADF) micrograph at the wet oxidation front and the corresponding STEM-EDS elemental mapping of arsenic (purple) and oxygen (cyan). One typical oxidation front is marked in the optical micrograph around one PC cavity in the inset. (e) STEM-EELS elemental mapping revealing the presence of oxygen at the cross-section of a PC structure.

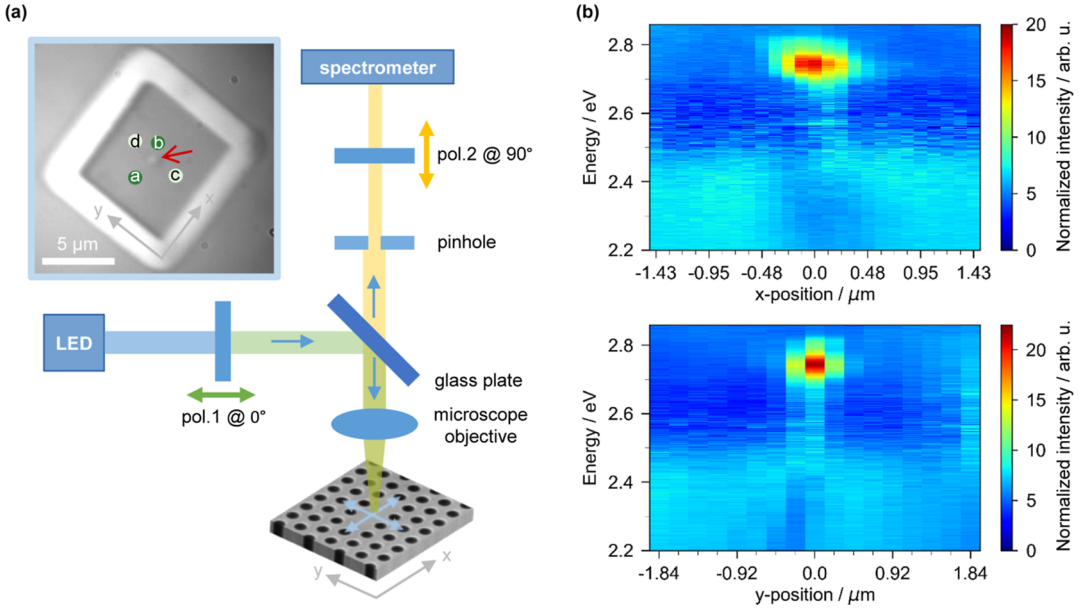

Figure 3. (a) Schematic drawing of the cross-polarized RS spectroscopy setup. The inset shows the spatial-dependent reflection map of a PC cavity subject to *x*- and *y*-line scans, with the starting/ending scanning positions marked as "*a*"/"*b*" and "*c*"/"*d*" inside the circles (with the diameter of the circles corresponding to the spatial resolution obtained with our pinhole). The cavity region is marked with a red arrow. (b) Normalized cross-polarized RS spectra of *x*- and *y*-line scans.

To investigate the influence of wet oxidation on the sample's strain condition, we measured PL spectra from the same sample at untreated and wet-oxidized regions, as indicated by the black and red spots in the inset of Figure 2c, respectively. Note that the diameters of the spots reflect the approximate circular collection area with about 1 μm diameter on the sample. The measurement was carried out at 10 K under above-band excitation with a 377 nm continuous-wave laser and with a spectrometer equipped with a 600 lines/mm blazed grating. The PL spectra in Figure 2c reveal a two-peak structure in the excitonic transition region of

https://doi.org/10.1021/acsphotonics.4c00340
ACS Photonics 2024, 11, 3545−3553

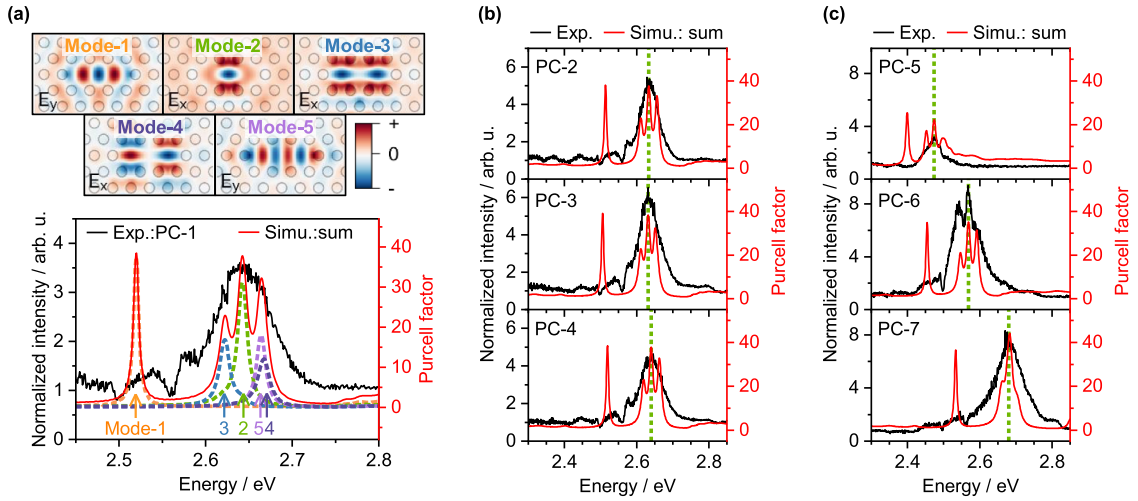

Figure 4. Normalized cross-polarized RS spectra of several measured PC cavities and the corresponding simulated sum spectra of the Purcell factor. For the structure PC-1, the mode profile of the dominant electric field and the individual contribution of Purcell factor from each present mode are shown. The structures are (a) PC-1 with $L = (181 \pm 4)$ nm and $R = 0.274 \pm 0.013$ (b) Three PC cavities with similar parameters, PC-2/PC-3/PC-4: $L = (181 \pm 3)$ nm/(181 ± 4) nm/(181 ± 4) nm, $R = 0.269 \pm 0.014/0.276 \pm 0.017/0.272 \pm 0.017$. (c) Three PC cavities with similar lattice constants but different radii ratios, PC-5/PC-6/PC-7: $L = (186 \pm 5)$ nm/(186 ± 3) nm/(185 ± 3) nm, $R = 0.223 \pm 0.020/0.264 \pm 0.014/0.303 \pm 0.011$. The mode energy of the dominant mode 2 is marked with the green dashed lines in (b) and (c).

the ZnSe QW, where the peaks at 2.840 and 2.832 eV, respectively, corresponds to the emission from neutral and charged excitons in the QW. The charged exciton peak has a comparable intensity as the neutral exciton peak, which is most likely caused by residual n-type background doping in our growth chamber. Remarkably, the PL peak positions shown in Figure 2c remain at the same spectral energy for both untreated and wet-oxidized regions, which indicates complete preservation of the compressive strain after the wet oxidation process.

Furthermore, for a better understanding of the influence of the fabrication process on the semiconductor properties, we conducted scanning transmission electron microscopy analysis of a typical PC cavity after fabrication. For analysis preparation, two lamellas across a PC structure and across a wet oxidation front in the sample are lifted out using focused ion beam milling. Figure 2d shows the cross-sectional HAADF micrograph of the wet oxidation front and the corresponding elemental maps of arsenic and oxygen obtained by energy dispersive spectroscopy (EDS). From the change in contrast across the middle layer shown in the HAADF micrograph, the material changes across the oxidation front. Since arsenic is not found in the EDS map on the oxidized side of the oxidation front, the transformation of AlAs into amorphous oxide (most probably aluminum hydroxide[38,43]) is confirmed. For convenience, we refer to this oxide layer as AlO_x in the following discussion. Figure 2e shows the elemental mapping of oxygen by electron energy loss spectroscopy (EELS) at the cross section of the PC structure. The sidewalls of the etched holes in the ZnSe/ZnMgSe layers show the presence of oxygen, indicating a certain degree of ZnMgSe oxidation. This is a side effect that results from the wet oxidation and the Cr-removal steps with O_2 and Cl_2/O_2 plasma. This oxidation impacts the refractive index of the material and, therefore, alters the cavity mode energy and Q-factor of the fabricated PC cavities. As discussed in the following analysis, this effect is taken into account when simulating PC cavities.

Following our PC cavity design and sample preparation, the subsequent optical characterization of the PC cavities is conducted using a cross-polarized RS spectroscopy setup,[4,44] as schematically illustrated in Figure 3a. In this setup, excitation is performed using a white light LED and the first polarizer sets the polarization at a 45° angle tilt to the cavity direction (long axis of the L3 defect) and in the sample plane. On one hand, this ensures excitation and collection of the cavity modes, which are polarized either parallel or perpendicular to the cavity axis (as discussed below in Figure 4a). On the other hand, a second polarizer, rotated by 90° relative to the first one, ensures that the directly reflected light from the sample surface is filtered out. In addition, we use a microscope objective with a large numerical aperture of 0.9 to attain a large collection angle, which circumvents the complexities associated with the far-field projection of various cavity modes. A pinhole with a diameter of 100 μm is implemented as a spatial filter for the region of interest, and a blazed grating with 150 lines/mm is chosen in the spectrometer to resolve a large spectral range covering the cavity modes of various PC cavity designs. The experiments are carried out at a temperature of 10 K.

In order to verify the presence of cavity modes, we first performed line scans in the x- and y-directions across a PC cavity (with dimensions $L = (186 \pm 4)$ nm, $R = 0.308 \pm 0.016$). A reflection map of the investigated PC cavity is shown as an inset in the left upper corner of Figure 3a, where the starting/ending positions of the scans are labeled as "a"/"b" and "c"/"d" inside the circles, and the circle size represents the spatial resolution obtained with our pinhole. The results of the line scans in both directions are shown in Figure 3b, with the obtained RS spectra normalized to one reference spectrum taken far from the cavity region. In the center of the cavity region, a resonant signal is visible at an energy of 2.727 eV, which we attribute to the presence of specific cavity modes.

For a specific PC cavity, detailed mode analysis from the simulation was carried out. Figure 4a depicts the background-normalized RS spectrum of a single PC cavity ($L = (181 \pm 4)$ nm and $R = 0.274 \pm 0.013$) together with the simulated mode spectra and Purcell factors of different modes (colored dashed spectra), as well as the overall response given by the sum of all modes (red spectrum). In the simulation altogether, 5 modes are revealed for this particular PC cavity in the investigated spectral region. The highest energy mode 1 is spectrally separated, while

https://doi.org/10.1021/acsphotonics.4c00340
ACS Photonics 2024, 11, 3545−3553

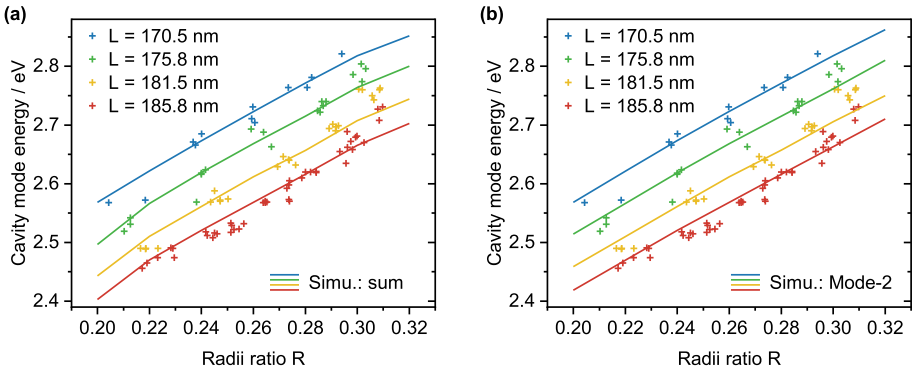

Figure 5. Cavity mode energies extracted from experimental spectra of various PC cavities. (a) Cluster peak energies obtained by summing up the mode profiles of modes 2−5 versus radii ratio. (b) Peak energy of the dominant mode 2 versus radii ratio. Dots correspond to the experimentally measured energies, and lines are obtained from the theoretical simulations using the corresponding lattice constants labeled in the legend of the diagrams.

modes 2−5 form a cluster with closely merged mode energies. The electric field distribution of each mode is also shown in Figure 4a, where E_y is the dominant electric field for mode 1 and mode 5 and E_x that for the other modes, respectively. The electric field of mode 1 is strongly concentrated in the cavity region, unlike that of the other modes, which is more delocalized and penetrates into neighboring air holes. This observation accounts for the lowest cavity mode photon energy of mode 1 in the simulation. Further theoretical investigation of the far-field projections reveals that each mode's emission is polarized with a polarization angle aligned with the dominant electric field direction, which renders the measurement with the above-described cross-polarized RS spectroscopy setup feasible. For the simulation, the ZnMgSe dispersion relation was scaled by a factor of (93 ± 1)% (see Supporting Information Section S2 for details) so that the simulated peak energies (colored spectra in Figure 4a) match the experimental one (black spectrum). This modification is justified under consideration of the process-related oxidation of ZnMgSe into ZnMgSeO, as previously discussed (following the STEM-EELS results in Figure 2e), which would reduce the overall effective refractive index in the structure. Additionally, in our observation, the broad RS signal region around 2.65 eV can be attributed to the superposition of a cluster of cavity modes 2−5, as underlined by the simulations. The experimentally obtained RS spectra (black curves) in Figure 4 follow the general trend of the simulation results. However, the individual modes 2−5 in the cluster cannot be resolved in the RS spectra, which indicates a substantially lower measured *Q*-factor of all modes. A more detailed analysis of the observed *Q* factor of the cluster and the comparison with the simulation results are presented in Section S5 of the Supporting Information. Considering the line width of the envelope function of the mode cluster for both the experimental and simulated data sets, the measured *Q*-factors are in the range of 30 to 60, while the simulated ones spawn in the range of 50 to 120. Hence, the experimental *Q*-factors are roughly a factor of 2 smaller. We believe that this reduction is a consequence of substantial surface roughness of the hole-sidewalls, which leads to additional photon loss via surface scattering.

Notably, mode 1 does not seem to appear in the recorded spectra, while at least a subset of modes 2−5 are observed. We attribute this to the higher *Q*-factor of mode 1 and to the loss channel toward the bottom of the II/VI stack resulting from the reduced index contrast at the boundary to the AlO_x. The *k*-vector distribution of mode 1 of L3 cavities is mostly outside of the light cone of vacuum, suppressing coupling to free space.[8] Rather, light is primarily lost via downward emission toward the GaAs substrate once the oxide undercladding is introduced. In a suspended membrane, the higher *Q*-factor may allow the mode to build to sufficient intensities to enable substantial free-space coupling via interference effects. Here, however, the reduced *Q*-factor is expected to prevent cavity mode buildup that is sufficiently strong to overcome the poor coupling toward the top of the structure. To make matters worse, the far-field emission pattern of mode 1 is composed of emission lobes at a large angle relative to the surface normal of the chip.[45] This makes it both harder to excite the mode via a vertically incident Gaussian beam, as used in the experimental setup implemented here, and harder to record its emission via a collection system with a finite numerical aperture. Modes 2−4, on the other hand, are expected to present an emission profile with a strong, vertically emitted beam,[45] which facilitates both excitation and detection.

To address the influence of fabrication tolerances and microscopic PC designs on the experimentally observed resonant signals, normalized experimental spectra of six PC cavities are shown in Figure 4b,c, alongside their corresponding simulated cavity responses and Purcell factors. The best agreement between simulation and experimental results was again found by using the previously determined refractive index scaling factor of (93 ± 1)% of ZnMgSeO. For all six investigated cavities, mode 2 (its energy marked by a green dashed line) is the dominant mode in the cluster. Taking a closer look, Figure 4b shows the RS spectra of three PC cavities (PC-2, PC-3, and PC-4) of the same design but with slight parameter variations, which stem from fabrication tolerances (lattice constant L = (181 ± 3) nm, (181 ± 4) nm, and (181 ± 4) nm and radii ratio $R = 0.269 \pm 0.014$, 0.276 ± 0.017, and 0.272 ± 0.017, as determined from the respective SEM micrographs, where the obtained lattice constants closely match the intended design of 180 nm). The experimental cavity mode energies are extracted from the peak positions, and their values vary only slightly (2.629, 2.632, and 2.646 eV), which confirms substantial robustness of the cavity mode energy against fabrication tolerances. On the other hand, Figure 4b shows spectra of three PC cavities (PC-5, PC-6, and PC-7) selected from different designs with nearly equal lattice constants close to the designed value of 185 nm, but having distinct radii ratios [L = (186 ± 5) nm, (186 ± 3) nm, and (185 ± 3) nm; $R = 0.223 \pm 0.020$, 0.264 ± 0.014, and 0.303 ± 0.011]. The experimentally observed cavity mode energy significantly blue-shifts with increasing hole radius (2.474, 2.568, and 2.670

https://doi.org/10.1021/acsphotonics.4c00340
ACS Photonics 2024, 11, 3545−3553

eV), as expected from the corresponding simulations. This result demonstrates the possibility of tuning the cavity mode energy over a large spectral range, which can be applied in the future to bring the cavity mode close to resonance with the QW emission for Purcell enhancement.

In order to gain a more comprehensive insight into the PC cavities and especially to quantify the dispersion relation in our heterostructures, including the above-mentioned formation of ZnMgSeO, we extensively investigated nearly 100 individual PC cavities with varying lattice constants and radii ratios and extracted the experimental cavity mode energies from the measured RS spectra. In Figure 5, the experimentally determined mode energies are plotted versus the radii ratios (dots). For each measured data point, the real radii ratio was individually determined by extraction of the average diameter of the holes and their mean distance from the SEM micrographs of the investigated PC cavities. All obtained data sets were assigned to four main groups of structures with different designed lattice constants. Cavity mode simulations were performed using the average value of the determined lattice constants for each group [(170.5 ± 0.4) nm (blue), (175.8 ± 0.3) nm (green), (181.5 ± 0.4) nm (yellow), and (185 8 ± 0.5) nm (red)] and with radii ratios ranging from 0.20 to 0.32. Experimental data points and simulation results are compared in Figure 5a with respect to the cluster peak energy as obtained by summing up the mode profiles of modes 2−5 and in Figure 5b, when only the spectral energy of the dominant mode 2 is considered, respectively. In both cases, the experimental data are in good agreement with the simulated dependence of the radii ratio. Only a small deviation can be seen in the case of radii ratios larger than 0.30, which could be due to a slight underestimation of the degree of ZnMgSe oxidation for large radii ratios in the model. In this case, the smaller volume of ZnMgSe material between the air holes may ease the oxidation process, requiring an additional correction of the scaling factor for the ZnMgSe dispersion relation.

The observation of cavity modes, which spans a broad range of cavity mode energy from 2.45 to 2.821 eV, proves the successful implementation of 2D PC cavities in ZnSe QW heterostructures. At the same time, the excellent agreement between our simulation and experimental results demonstrates the pertinence of our simulation model by using our quantified dispersion relation of ZnMgSeO.

CONCLUSIONS

In this work, we demonstrate the implementation of 2D PC cavities within ZnSe QW heterostructures, as tailored for the blue-green spectral range. To the best of our knowledge, no prior investigation of 2D PC cavities has been reported in this specific material system. In our innovative approach, the QW heterostructure is grown on top of an AlAs buffer layer, which then is postgrowth wet-oxidized into AlO_x. This technique is a mandatory requirement to provide excellent mechanical stability as well as sufficient optical confinement in the vertical direction via index guiding.

Detailed analysis using SEM revealed excellent structural properties of the fabricated PC cavities, with steep side walls of the etched holes signifying remarkable etching anisotropy. This is particularly noteworthy considering the small characteristic length scale, represented by etched holes with diameters in the range of (70−115) nm. The applied elemental mapping techniques, namely EDS and EELS, not only confirmed the complete wet-oxidation of AlAs into AlO_x, but also revealed partial oxidation of the II−VI heterostructure. In particular, oxidation of the ZnMgSe barriers leads to the formation of ZnMgSeO and alters the corresponding dispersion relation. The optical characterization of fabricated PC cavities using cross-polarized RS spectroscopy verified the existence of cavity modes in the central PC cavity region, of which the energy can be tuned over a broad spectral range of (2.456−2.821) eV, depending on the microscopic PC design. Moreover, we quantified the effective dispersion relation of the partially oxidized QW heterostructure and determined a scaling factor of (93 ± 1)% by fitting the measured cavity mode energies with simulation results performed with a FDTD solver.

The obtained results represent a solid experimental and theoretical basis for further investigations of PC cavities in the II−VI semiconductor material system. Those may cover, for example, interaction between cavity and QW emission, the enhancement of Purcell factors, or tailoring of the angular far-field projection of the cavity modes.

ASSOCIATED CONTENT

Supporting Information

The Supporting Information is available free of charge at https://pubs.acs.org/doi/10.1021/acsphotonics.4c00340.

Reciprocal space map of the pristine layer stack, dispersion relations of ZnMgSe and AlO_x, sample fabrication, circle fitting of SEM micrographs, and analysis of the *Q*-factors. (PDF)

AUTHOR INFORMATION

Corresponding Authors

Siqi Qiao − *Peter Grünberg Institute (PGI-9), Forschungszentrum Jülich GmbH, 52428 Jülich, Germany; JARA-Fundamentals of Future Information Technology, Jülich-Aachen Research Alliance, 52074 Aachen, Germany*; Email: s.qiao@fz-juelich.de

Alexander Pawlis − *Peter Grünberg Institute (PGI-9), Forschungszentrum Jülich GmbH, 52428 Jülich, Germany; Peter Grünberg Institute (PGI-10), Forschungszentrum Jülich GmbH, 52428 Jülich, Germany; JARA-Fundamentals of Future Information Technology, Jülich-Aachen Research Alliance, 52074 Aachen, Germany*; orcid.org/0000-0002-3394-0707; Email: a.pawlis@fz-juelich.de

Authors

Nils von den Driesch − *Peter Grünberg Institute (PGI-10), Forschungszentrum Jülich GmbH, 52428 Jülich, Germany; JARA-Fundamentals of Future Information Technology, Jülich-Aachen Research Alliance, 52074 Aachen, Germany*; orcid.org/0000-0003-0169-6110

Xi Chen − *Department of Materials Science and Engineering, Massachusetts Institute of Technology, Cambridge, Massachusetts 02139, United States*

Stefan Trellenkamp − *Helmholtz Nano Facility, Forschungszentrum Jülich GmbH, 52428 Jülich, Germany*

Florian Lentz − *Helmholtz Nano Facility, Forschungszentrum Jülich GmbH, 52428 Jülich, Germany*

Christoph Krause − *Peter Grünberg Institute (PGI-10), Forschungszentrum Jülich GmbH, 52428 Jülich, Germany*

Benjamin Bennemann − *Peter Grünberg Institute (PGI-10), Forschungszentrum Jülich GmbH, 52428 Jülich, Germany*

Thorsten Brazda − *Peter Grünberg Institute (PGI-9), Forschungszentrum Jülich GmbH, 52428 Jülich, Germany*

https://doi.org/10.1021/acsphotonics.4c00340
ACS Photonics 2024, 11, 3545−3553

Jeremy Witzens − *Institute of Integrated Photonics, RWTH Aachen University, 52074 Aachen, Germany;* orcid.org/0000-0002-2896-7243

James M. LeBeau − *Department of Materials Science and Engineering, Massachusetts Institute of Technology, Cambridge, Massachusetts 02139, United States;* orcid.org/0000-0002-7726-3533

Complete contact information is available at: https://pubs.acs.org/10.1021/acsphotonics.4c00340

Funding

This work is supported by Deutsche Forschungsgemeinschaft (DFG, German Research Foundation) under Germany's Excellence Strategy—Cluster of Excellence: Matter and Light for Quantum Computing (ML4Q) (EXC 2004 1-390534769). X.C. and J.L. gratefully acknowledge support from the Air Force Office of Scientific Research (FA9550-20-0066).

Notes

The authors declare no competing financial interest.

■ ACKNOWLEDGMENTS

The authors gratefully acknowledge the technical support by the staff of the Helmholtz Nano Facility (HNF) of Forschungszentrum Jülich in the fabrication process as well as our colleagues in PGI-9 and PGI-10.

■ REFERENCES

(1) Happ, T. D.; Tartakovskii, I. I.; Kulakovskii, V. D.; Reithmaier, J. P.; Kamp, M.; Forchel, A. Enhanced light emission of $In_xGa_{1-x}As$ quantum dots in a two-dimensional photonic-crystal defect microcavity. *Phys. Rev. B: Condens. Matter Mater. Phys.* **2002**, *66*, 041303.

(2) Riedrich-Möller, J.; Arend, C.; Pauly, C.; Mücklich, F.; Fischer, M.; Gsell, S.; Schreck, M.; Becher, C. Deterministic coupling of a single silicon-vacancy color center to a photonic crystal cavity in diamond. *Nano Lett.* **2014**, *14*, 5281−5287.

(3) Chang, W. H.; Chen, W. Y.; Chang, H. S.; Hsieh, T. P.; Chyi, J. I.; Hsu, T. M. Efficient single-photon sources based on low-density quantum dots in photonic-crystal nanocavities. *Phys. Rev. Lett.* **2006**, *96*, 117401.

(4) Liapis, A. C.; Gao, B.; Siddiqui, M. R.; Shi, Z.; Boyd, R. W. On-chip spectroscopy with thermally tuned high-Q photonic crystal cavities. *Appl. Phys. Lett.* **2016**, *108*, 021105.

(5) Lončar, M.; Yoshie, T.; Scherer, A.; Gogna, P.; Qiu, Y. Low-threshold photonic crystal laser. *Appl. Phys. Lett.* **2002**, *81*, 2680−2682.

(6) Wu, X.; Yamilov, A.; Liu, X.; Li, S.; Dravid, V. P.; Chang, R. P. H.; Cao, H. Ultraviolet photonic crystal laser. *Appl. Phys. Lett.* **2004**, *85*, 3657−3659.

(7) Ohta, R.; Ota, Y.; Nomura, M.; Kumagai, N.; Ishida, S.; Iwamoto, S.; Arakawa, Y. Strong coupling between a photonic crystal nanobeam cavity and a single quantum dot. *Appl. Phys. Lett.* **2011**, *98*, 173104.

(8) Akahane, Y.; Asano, T.; Song, B. S.; Noda, S. High-Q photonic nanocavity in a two-dimensional photonic crystal. *Nature* **2003**, *425*, 944−947.

(9) Chalcraft, A. R.; Lam, S.; O'Brien, D.; Krauss, T. F.; Sahin, M.; Szymanski, D.; Sanvitto, D.; Oulton, R.; Skolnick, M. S.; Fox, A. M.; Whittaker, D. M.; Liu, H. Y.; Hopkinson, M. Mode structure of the L3 photonic crystal cavity. *Appl. Phys. Lett.* **2007**, *90*, 241117.

(10) Shih, M.-H.; Mock, A.; Bagheri, M.; Suh, N.-K.; Farrell, S.; Choi, S.-J.; O'Brien, J. D.; Dapkus, P. D. Photonic crystal lasers in InGaAsP on a SiO2/Si substrates and its thermal impedance. *Opt. Express* **2007**, *15*, 227.

(11) Triviño, N. V.; Butté, R.; Carlin, J. F.; Grandjean, N. Continuous wave blue lasing in iii-nitride nanobeam cavity on silicon. *Nano Lett.* **2015**, *15*, 1259−1263.

(12) Néel, D.; Sergent, S.; Mexis, M.; Sam-Giao, D.; Guillet, T.; Brimont, C.; Bretagnon, T.; Semond, F.; Gayral, B.; David, S.; Checoury, X.; Boucaud, P. AlN photonic crystal nanocavities realized by epitaxial conformal growth on nanopatterned silicon substrate. *Appl. Phys. Lett.* **2011**, *98*, 261106.

(13) Arita, M.; Ishida, S.; Kako, S.; Iwamoto, S.; Arakawa, Y. AlN air-bridge photonic crystal nanocavities demonstrating high quality factor. *Appl. Phys. Lett.* **2007**, *91*, 051106.

(14) Choi, Y.-S.; Hennessy, K.; Sharma, R.; Haberer, E.; Gao, Y.; Denbaars, S. P.; Nakamura, S.; Hu, E. L.; Meier, C. GaN blue photonic crystal membrane nanocavities. *Appl. Phys. Lett.* **2005**, *87*, 243101.

(15) Meier, C.; Hennessy, K.; Haberer, E. D.; Sharma, R.; Choi, Y.-S.; McGroddy, K.; Keller, S.; DenBaars, S. P.; Nakamura, S.; Hu, E. L. Visible resonant modes in GaN-based photonic crystal membrane cavities. *Appl. Phys. Lett.* **2006**, *88*, 031111.

(16) Hoffmann, S. P.; Albert, M.; Meier, C. Fabrication of fully undercut ZnO-based photonic crystal membranes with 3D optical confinement. *Superlattices Microstruct.* **2016**, *97*, 397−408.

(17) Hoffmann, S. P.; Albert, M.; Weber, N.; Sievers, D.; Förstner, J.; Zentgraf, T.; Meier, C. Tailored UV Emission by Nonlinear IR Excitation from ZnO Photonic Crystal Nanocavities. *ACS Photonics* **2018**, *5*, 1933−1942.

(18) Pawlis, A.; Berstermann, T.; Brüggemann, C.; Bombeck, M.; Dunker, D.; Yakovlev, D. R.; Gippius, N. A.; Lischka, K.; Bayer, M. Exciton states in shallow ZnSe/(Zn,Mg)Se quantum wells: Interaction of confined and continuum electron and hole states. *Phys. Rev. B: Condens. Matter Mater. Phys.* **2011**, *83*, 115302.

(19) Kutovyi, Y.; Jansen, M. M.; Qiao, S.; Falter, C.; Von Den Driesch, N.; Brazda, T.; Demarina, N.; Trellenkamp, S.; Bennemann, B.; Grützmacher, D.; Pawlis, A. Efficient Single-Photon Sources Based on Chlorine-Doped ZnSe Nanopillars with Growth Controlled Emission Energy. *ACS Nano* **2022**, *16*, 14582−14589.

(20) Ruth, M.; Finke, A.; Schmidt, G.; Reuter, D.; Scholz, S.; Ludwig, A.; Wieck, A. D.; Pawlis, A. Optical properties of strain-compensated CdSe/ZnSe/(Zn,Mg)Se quantum well microdisks. *Opt. Express* **2015**, *23*, 29079.

(21) Finke, A.; Ruth, M.; Scholz, S.; Ludwig, A.; Wieck, A. D.; Reuter, D.; Pawlis, A. Extending the spectral range of CdSe/ZnSe quantum wells by strain engineering. *Phys. Rev. B: Condens. Matter Mater. Phys.* **2015**, *91*, 035409.

(22) Sanaka, K.; Pawlis, A.; Ladd, T. D.; Lischka, K.; Yamamoto, Y. Indistinguishable photons from independent semiconductor nanostructures. *Phys. Rev. Lett.* **2009**, *103*, 053601.

(23) Karasahin, A.; Pettit, R. M.; Von Den Driesch, N.; Jansen, M. M.; Pawlis, A.; Waks, E. Single quantum emitters with spin ground states based on Cl bound excitons in ZnSe. *Phys. Rev. A* **2022**, *106*, L030402.

(24) Pettit, R. M.; Karasahin, A.; Von Den Driesch, N.; Jansen, M. M.; Pawlis, A.; Waks, E. Correlations between Cascaded Photons from Spatially Localized Biexcitons in ZnSe. *Nano Lett.* **2022**, *22*, 9457−9461.

(25) Sanaka, K.; Pawlis, A.; Ladd, T. D.; Sleiter, D. J.; Lischka, K.; Yamamoto, Y. Entangling single photons from independently tuned semiconductor nanoemitters. *Nano Lett.* **2012**, *12*, 4611−4616.

(26) Sleiter, D. J.; Sanaka, K.; Kim, Y. M.; Lischka, K.; Pawlis, A.; Yamamoto, Y. Optical pumping of a single electron spin bound to a fluorine donor in a ZnSe nanostructure. *Nano Lett.* **2013**, *13*, 116−120.

(27) Kim, Y. M.; Sleiter, D.; Sanaka, K.; Reuter, D.; Lischka, K.; Yamamoto, Y.; Pawlis, A. Optically controlled initialization and read-out of an electron spin bound to a fluorine donor in ZnSe. *Curr. Appl. Phys.* **2014**, *14*, 1234−1239.

(28) Heisterkamp, F.; Zhukov, E. A.; Greilich, A.; Yakovlev, D. R.; Korenev, V. L.; Pawlis, A.; Bayer, M. Longitudinal and transverse spin dynamics of donor-bound electrons in fluorine-doped ZnSe: Spin inertia versus Hanle effect. *Phys. Rev. B* **2015**, *91*, 235432.

(29) Jiang, Y.; Pettit, R. M.; den Driesch, N.; Pawlis, A.; Waks, E. Cavity-Enhanced Single-Photon Emission from a Single Impurity-Bound Exciton in ZnSe. *ACS Photonics* **2024**, *11*, 1103−1108.

(30) Pawlis, A.; Khartchenko, A.; Husberg, O.; As, D. J.; Lischka, K.; Schikora, D. Large room temperature Rabi-splitting in a ZnSe/(Zn,Cd)Se semiconductor microcavity structure. *Solid State Commun.* **2002**, *123*, 235−238.

(31) Curran, A.; Morrod, J. K.; Prior, K. A.; Kar, A. K.; Warburton, R. J. Exciton−photon coupling in a ZnSe-based microcavity fabricated using epitaxial liftoff. *Semicond. Sci. Technol.* **2007**, *22*, 1189−1192.
(32) Sebald, K.; Seyfried, M.; Klembt, S.; Bley, S.; Rosenauer, A.; Hommel, D.; Kruse, C. Strong coupling in monolithic microcavities with ZnSe quantum wells. *Appl. Phys. Lett.* **2012**, *100*, 161104.
(33) Phillips, P. L.; Knight, J. C.; Mangan, B. J.; Russell, P. S. J.; Charlton, M. D.; Parker, G. J. Near-field optical microscopy of thin photonic crystal films. *J. Appl. Phys.* **1999**, *85*, 6337−6342.
(34) Chow, E.; Lin, S. Y.; Johnson, S. G.; Villeneuve, P. R.; Joannopoulos, J. D.; Wendt, J. R.; Vawter, G. A.; Zubrzycki, W.; Hou, H.; Alleman, A. Three-dimensional control of light in a two-dimensional photonic crystal slab. *Nature* **2000**, *407*, 983−986.
(35) Tokushima, M.; Kosaka, H.; Tomita, A.; Yamada, H. Lightwave propagation through a 120° sharply bent single-line-defect photonic crystal waveguide. *Appl. Phys. Lett.* **2000**, *76*, 952−954.
(36) Liu, X.; Furdyna, J. K. Optical dispersion of ternary II-VI semiconductor alloys. *J. Appl. Phys.* **2004**, *95*, 7754−7764.
(37) Puls, J.; Rabe, M.; Siarkos, A.; Henneberger, F. Excitonic properties of ZnSe/(Zn, Mg)Se quantum wells: A model study of the tensile-strain situation. *Phys. Rev. B* **1998**, *57*, 14749−14757.
(38) Hirai, Y.; Yamada, T.; Kondow, M.; Ishikawa, F. Characterization of the oxide film obtained by wet oxidation of Al-Rich AlGaAs. *Jpn. J. Appl. Phys.* **2012**, *51*, 02BG10.
(39) Bek, A.; Aydinli, A.; Champlain, J. G.; Naone, R.; Dagli, N. A study of wet oxidized Al/sub x/Ga/sub 1-x/As for integrated optics. *IEEE Photonics Technol. Lett.* **1999**, *11*, 436−438.
(40) Palik, E. D. *Handbook of Optical Constants of Solids*; Academic Press, 1997; pp 429−443.
(41) MacDougal, M. H.; Zhao, H.; Steier, W. H.; Dapkus, P. D.; Ziari, M. Wide-bandwidth distributed Bragg reflectors using oxide/GaAs multilayers. *Electron. Lett.* **1994**, *30*, 1147−1149.
(42) Takamori, T.; Takemasa, K.; Kamijoh, T. Interface structure of selectively oxidized AlAs/GaAs. *Appl. Phys. Lett.* **1996**, *69*, 659−661.
(43) Li, R. Y.; Wang, Z. G.; Xu, B.; Jin, P.; Guo, X.; Chen, M. Interface of wet oxidized AlGaAs/GaAs distributed Bragg reflectors. *Appl. Phys. A: Mater. Sci. Process.* **2006**, *86*, 19−22.
(44) McCutcheon, M. W.; Rieger, G. W.; Cheung, I. W.; Young, J. F.; Dalacu, D.; Frédérick, S.; Poole, P. J.; Aers, G. C.; Williams, R. L. Resonant scattering and second-harmonic spectroscopy of planar photonic crystal microcavities. *Appl. Phys. Lett.* **2005**, *87*, 221110.
(45) Rickert, L.; Reithmaier, J. P.; Benyoucef, M. Telecom wavelength InP-based L3 photonic crystal cavities: Properties of the cavity ground mode. *AIP Conf. Proc.* **2020**, *2241*, 020004.

https://doi.org/10.1021/acsphotonics.4c00340
ACS Photonics 2024, 11, 3545−3553